

***Final Draft***  
**of the original manuscript:**

Martinson, P.; Daneshpour, S.; Kocak, M.; Riekehr, S.; Staron, P.:  
**Residual stress analysis of laser spot welding of steel sheets**  
In: Materials and Design (2009) Elsevier

DOI: 10.1016/j.matdes.2009.03.041

# Residual Stress Analysis of Laser Spot Welding of Steel Sheets

P. Martinson<sup>a,b</sup>, S. Daneshpour<sup>a</sup>, M. Koçak<sup>a</sup>, S. Riekehr<sup>a</sup>, P. Staron<sup>a</sup>

<sup>a</sup> GKSS Research Centre, Institute of Materials Research, Geesthacht, Germany

<sup>b</sup> University of Waterloo, Dep. of Mechanical and Mechatronics Engineering, Waterloo, Canada

## Abstract

Experimental and numerical studies were conducted to characterize laser and resistance spot welds to gain an understanding of load carrying capacity, temperature distributions and residual stress states of different joint geometries used in automotive industry. Different laser spot weld (LSW) path geometries are compared with conventional resistance spot welds to find the residual stress distributions in each. It was found out that the weld region in LSW has been surrounded by a compressive region which has higher compressive stress values and bigger size than that of resistance spot welds. Simulations showed good agreement with experimental temperature distributions, and can qualitatively predict the residual stress distributions in each of the weld geometries. The thermal history at known failure locations within the welds, and the influence of the weld geometries on cooling rate are also discussed.

*Keywords:* Laser Spot Welding; Resistance Spot Welding; Residual Stress; Thermal Analysis; Finite Element Analysis; Heat Source Model.

## 1 Introduction

Resistance Spot Welding (RSW) remains to be the most widely-used joining method in the automotive industry [1]. However, Laser Spot Welding (LSW) provides a flexible alternative to RSW with the benefits of low distortion due to concentrated heat source, and requires only line-of-sight (with one side of the area to be welded) fabrication, allowing for access to more difficult-

to-reach areas. Further advances, such as the remote welding method [2] will allow even higher rates of throughput, which is of great importance when considering the high volumes and quantities of welds associated with automobile manufacture.

Simulation of welding processes has its roots in the first analytical welding models proposed by Rosenthal [3], which approximated the heat source as a single point or line through the material. Over time, models with a distributed heat source across a surface [4] and throughout a 3D volume [5] were developed, making the accurate modelling of a range of different heat sources, including laser beam welding (LBW), possible. Mazumder and Steen [6] proposed a FE- method with specific considerations for the keyhole mode of laser welding, and work in understanding and simulating the physical phenomena found within the fusion zone was continued by Sudnik et. al [7]. Significant increases in computational power in the last two decades have made finite element analysis using 2D and 3D meshes possible, as well as the prediction of residual stresses in and around the welded region. Recent simulations using commercial software such as ABAQUS [8, 9], ANSYS [10], and the more function- specific SYSWELD [11,12] have all been successful in determining residual stresses, both for LBW and other welding processes.

Improved understanding of the fatigue behaviour, in connection with residual stresses, is an extremely important subject particularly for newly developed welding processes such as LSW. Previous work [13] has compared the fatigue behaviour of resistance spot welds and laser spot welds of dissimilar materials, including advanced high-strength steels (AHSS), while others have analysed different types of butt-welded specimens on a microstructural level [14]. Thermo-mechanical analysis of laser spot welding can provide useful information to improve the understanding of the cyclic behaviour of welded structures, and this information can lead to better damage-tolerant design of these structures. The present paper aims to determine the effect of different laser spot weld shapes on the residual stress state in comparison with the residual stress state found in resistance spot welds, primarily through an analysis of the residual stresses developed. Simulation of the LSW process using the ABAQUS FE suite was conducted alongside the experimental analysis, and comparisons of results will be presented. Fatigue performance of the different laser spot weld path geometries will be reported in the next communication due to the space available in this manuscript.

## 2 Experimental Procedure

Although the term Laser Spot Welding is used, welding occurs over a short continuous path, rather than at a single point, which is the case for resistance spot welds. This terminology was chosen to draw comparisons with RSW, which the LSW process was developed to produce welds of similar quality, while maintaining the same or possibly shorter cycle times. The variation of these paths, using different combinations of lines and circular or elliptical arcs, led to the development of the four weld geometries that were analysed.

### 2.1 Welding Path Geometries

The “Ring weld” geometry of LSW and nugget type of RSW were taken from our prior work [13], and would be used as the basis for comparison with other geometries. The start and end points of laser welds, which start point is often prone to failure due to low penetration and high cooling rate while end point is due to impurities pileup as a result of keyhole collapse, were located to one side of the circle, rather than in the centre, which was already seen to contain very high residual stresses. Although these regions are prone to failure, the “Ring” configuration mitigates the lack of penetration at the start point through overlap with the end point, which has full penetration. However, the issue of poor weld quality caused by keyhole collapse was not addressed, and so a new geometry was developed, where both the start and end points were protected from external forces by a layer of continuous welded material. This geometry was simply referred to as “Brezel”. This weld geometry can also be used to reduce the edge size of profiles used in automobile body-in-white, and lead to weight saving. Lastly, to determine the effect of the so called “protected endpoints” on fatigue behaviour, a third sample possessing the same geometry as the Brezel, without the first and last sections, was also used, and this was referred to as a “C- weld”. Dimensions were chosen to create Brezel welds with a short to long axis ratio of 0.5, and ensure that proper spacing was given on all sides of the start and end points. The radius of Ring welds was selected such that the weld seam length was equivalent to the Brezel welds. Fig. 1 shows photos and schematics of all laser spot weld configurations.

## 2.2 Welding Process and Specimen Preparation

All laser welds were made using a 3.3 kW Nd:YAG laser at the GKSS facilities, and further welding parameters of  $11 \text{ mms}^{-1}$  welding speed, +8.0 mm focal point, without shielding gas and filler wire were adjusted to obtain optimum joints, as judged by visual examination of the weld nugget surface appearance and sufficient weld penetration in the lower sheet of the overlap joints. 2.0 mm sheet thickness deep-drawn DC04 steel was chosen as the material on which all welds would be made, due to its prevalent use in the automotive industry. All welds were made on overlap specimens with dimensions given in Fig. 2. All geometries were centred in the middle of the 40 mm by 40 mm single overlap section of the specimen.

The resistance spot welds were made using a Schlatter 50 HZ AC stand alone spot welding machine at OCAS. Spot welds were made with a nugget diameter of approximately 7.0 mm (i.e.  $5\sqrt{t}$ ) in the centre of a 40 mm overlap between the sheets and with 42 mm between spots. The welded panels (1000 mm × 300 mm) were then cut to tensile-shear (TS) coupons. Typical joint cross section of resistance spot weld is shown in Fig. 3a.

## 2.3 Test Methodology

In order to evaluate temperature distributions of the different geometries, five thermocouples of type K with 0,5 mm diameter were placed around the weld paths, with four in the top sheet and one in the bottom sheet. Temperature values were recorded at 200 Hz and were used for comparison with simulations. A high speed video system was used to gain information about the length of the melt pool and the key hole diameter, which was used in the simulations, too. The videos were recorded with 1000 frame per second (fps).

Residual stress measurements using neutron diffraction was conducted on laser and resistance spot welded specimens. These were made along the major axes of the specimens, as shown in Fig. 2 and Fig. 3. Comprehensive descriptions of the method of residual stress analysis by diffraction can be found in the textbooks by Hauk [15], Fitzpatrick et al. [16], and Hutchings et al. [17]. Residual strain measurements were performed with the neutron diffractometer ARES-2 at the Geesthacht Neutron Facility (GeNF) at GKSS. Neutrons of 0.1637 nm wavelength from an elastically bent perfect Silicon (311) monochromator were used.

Diffraction methods for the determination of internal strains yield the sum of all strains and stresses present in the material, macro-stresses (type I stresses) as well as micro-stresses (type II and III stresses) [15]. Among the latter, inter-granular stresses, i.e. stresses between neighbouring grains, can play a significant role when the material has undergone plastic deformation. However, only macro-stresses are relevant for the comparison with FE model predictions; therefore, the influence of micro-stresses on the stress results determined by diffraction has to be minimized. The standard strategy for this is the use of lattice planes for the strain measurements, which are only weakly affected by inter-granular stresses and thus yield a good approximation for macro-stresses. Recommendations for such lattice planes exist for common materials [17, 18]; for bcc steel the (211) or (110) reflections are recommended. Therefore, in the present experiment the (211) diffraction peak of the  $\alpha$ -phase was recorded with an area detector at an angle of about  $2\theta = 89^\circ$ .

Diffraction peaks were measured with the samples oriented in three perpendicular directions for recording strains in  $x$ ,  $y$ , and  $z$  directions for all points on a scan line. Measured diffraction peaks were fitted with a Gaussian function. Strains  $\varepsilon_x$ ,  $\varepsilon_y$ , and  $\varepsilon_z$  were calculated from the measured peak positions  $\theta$  according to

$$\varepsilon = \frac{d - d_0}{d_0} = -\frac{\theta - \theta_0}{\tan\theta_0} \quad (1)$$

where  $d$  is the lattice parameter. The gauge volume is the volume in which the strains are measured and thus defines the spatial resolution of the method [17]. It is usually limited by the available source intensity. The resulting strains and stresses are mean values over this volume. The gauge volume was defined by Cd slits in the incoming and diffracted beam and had a cubic shape with nominal size  $1.5 \times 1.5 \times 1.5 \text{ mm}^3$ . The actual size is slightly larger because of the divergence of the incoming beam. With the used gauge volume, it can be distinguished between the two sheets in the overlapping region. The grain size of the material proved to be small enough to ensure good grain statistics with the used size of the gauge volume.

As is obvious from Eq. 1, the knowledge of the unstrained lattice parameter  $d_0$  at each measured point in the sample is required for the determination of strains. In a weld,  $d_0$  can

depend on the heat input experienced by the material during welding, because the lattice parameter can change e.g. with solute content. In this case,  $d_0$  was determined by assuming a plane stress state in the thin sheets. From the condition  $\sigma_z = 0$ ,  $d_0$  can be calculated for each point and the stresses  $\sigma_x$  and  $\sigma_y$  can be evaluated using a biaxial formula [19].

$$\sigma_{x,y} = \frac{E}{1-\nu^2} [\epsilon_{x,y} + \nu\epsilon_{y,x}] \quad (2)$$

In general, diffraction elastic constants have to be used for  $E$  and  $\nu$  which depend on the indices  $hkl$  of the reflection that are used for the strain measurement. The values  $E = 225$  GPa and  $\nu = 0.28$  were used for the (211) reflection of the iron  $\alpha$ -phase [15].

### 3 Simulation Details

3D FE simulations were performed for the Brezel, C-weld and Ring-weld geometries to determine the residual stresses in each, using ABAQUS FE software. Because the thermal cycles are reversed at the ends of the Brezel welds (applying pre-heating to the exterior arc near the start of the weld, and post-heating to the arc near the end point), and because of a temperature accumulation during the entire process, a symmetric model could not be used. A partially-coupled analysis, where first a thermal model, then a subsequent mechanical model using temperature data as an input, was used due to the considerable reduction in computation time when compared with a fully-coupled thermal-mechanical model.

#### 3.1 Finite Element Meshes

Fig. 4 shows the selected meshes for each geometry. DC3D8 brick elements, and a small amount of DC3D6 wedge elements were used from the ABAQUS element library [20] for each thermal analysis, while C3D8R (reduced integration brick elements) and some C3D6 (wedge elements) were used for the mechanical models. The air gap between the two sheets of the joint was modelled using a layer of elements between the two main sections (top and bottom sheets of joint) which was only 0.01mm thick. This was then divided into one region which was within the fusion zone and given the same properties as the rest of the base metal, and another which was outside the fusion zone, and would remain as a gap between the two sheets

throughout the process ( with zero conductivity). Elements in this region were given properties to eliminate expansion, and minimize forces acting on either sheet during the mechanical analysis.

Surface convection and radiation were both present in the thermal models, having coefficients of  $7.36 \times 10^{-07}$  and 0.25, respectively. Heat transfer across the gap between sheets was assumed to be zero, through manipulation of the properties of the Air Gap elements, but full conduction was allowed between sheets through the fusion zone, since these elements had the properties of the base material. Temperature dependant material properties, taken from SYSWELD material database, were used for the base material and isotropic hardening, containing two points in the plastic region at each temperature, was used to govern plastic behaviour of the material.

Mesh size was determined through a small sensitivity analysis involving Ring- weld models. Meshes containing 17500, 7500 and 4000 elements were all generated, and it was found that the results varied very little between the fine and medium-sized meshes, whereas computation time for the medium mesh was reduced by a factor of four. There were further reductions in computation time by using the coarse mesh, but the deviation in results from the other two cases was deemed too large, and thus it was not employed. Final meshes averaged 9000 elements for the three geometries used.

### 3.2 Heat Source Model

Several heat source models were considered to model the LSW process, with each being compared against experimental joint cross sections to find the best agreement. Among these, Goldak's Double Ellipsoid [15] was very capable, but the best agreement was found with the Conical Gaussian model (see Fig. 5), which is governed by Eq. 3:

$$q_{vol}(x,y,z) = q_0 \exp\left[-\frac{2(x^2 + y^2)}{r_z^2}\right] \quad (3a)$$

$$r_z = r_0 - \frac{z}{d}(r_0 - r_d) \quad (3b)$$



The parameters of the Conical Gaussian model were adjusted until the values shown in the Fig. 5 were reached, and these generated a weld cross section with dimensions very similar to the experimental results as shown in Fig. 6.

Initial simulations consisted of numerous steps, where the heat source was applied at a single point along the path in each step. This proved both difficult to adjust, and gave a discontinuous thermal history. This was replaced by a FORTRAN user subroutine, which is called as part of the DFLUX function. With this, a path for a moving reference point was generated according to the current geometry, and heat flux was calculated based on distance from this reference point to all nodes in the local area, according to the Eq. 3.

## **4 Results and Discussion**

### **4.1 Thermal Model Verification**

Results from the experimental temperature measurements were compared with temperature values from specific nodes in the thermal models, and in some cases the heat input parameters and step times in the simulation were adjusted to better correspond to the experimental results. Fig. 7 shows good agreement between the two, and also a common pattern of slightly lower values in the simulated results. One noteworthy discrepancy, which is most prevalent in the Ring- weld, is a much higher value for the experimental Probe 5 than its simulated counterpart, located in the centre of the ring, 0.6mm from the sheet interface in the bottom sheet. This shows that an assumption of zero conductance across the air gap may be an oversimplification. Other than this, most simulated values are very close to the experimental, and some amount of error is attributed to the fact that nodes do not align perfectly with the locations of temperature probes in the experimental specimens, and given the low conductivity of steel, variations in temperature can be seen across very small distances. The primary purpose of obtaining the thermal histories was to ensure the validity of any simulated residual stress results, but they were additionally used to find the cooling rates at specific points in each geometry.

## 4.2 Residual Stress and Cooling Rate Analyses

In Fig. 8, residual stress measurements for resistance spot weld of 7.0 mm nugget size are compared with that for Ring- weld geometry of LSW with a 7.0 mm ring diameter, along the directions shown in Fig. 3. In the comparison of the tangential residual stresses for RSW and LSW in Fig. 8a, LSW shows higher tensile residual stresses, limited to the area that is surrounded by the weld ring, than those found in the nugget for RSW. According to Fig. 8a, the weld region in LSW has been surrounded by a compressive region which is larger in magnitude than that of the RSW. Our previous studies on failure analysis of laser spot welds under static and cyclic loading [13, 21] reveal that the entire region of the weld ring has higher strength (overmatching) than the base material. This fact indicates the role of shielding effect of the strength overmatching on the weld region where the tensile residual stress exists (see Fig. 8) and hence the weld region will be protected from applied stress or strain. Compressive stresses in the region surrounding the laser spot weld (see Fig. 8a) serve to extend its fatigue life because of their tendency to close crack tips within this compressive region and prevent further propagation, as higher fatigue life of laser spot welds than that of resistance spot welds has been observed in our previous study [13]. Understanding which welding processes generate compressive residual stresses can be favourable when designing welded structures for cyclic loading and against brittle fracture.

Residual stresses for the top sheets of Brezel, C-weld and Ring-weld geometries are presented in Fig. 9, along the directions shown in Figs. 2 and 3. The main focus of this study is to know the fatigue performance of the different joint geometries and since typical plug type failure of spot welds has occurred in the area directly around the exterior of the weld ring [13], deviation between the experimental and simulated results in these areas was considered acceptable. Outside of this area, which extends 6.5 mm from the centre in both directions for Brezel and C-weld, and 5.5 mm from the centre for Ring-weld, the experimental and simulated results are very similar. Simulated results provide a good qualitative indication of maximum and minimum values, and predict the transition from compressive to tensile stresses very well. Residual stress measurements on the C-weld (Fig. 9b) is still ongoing and hence were not included into the diagram. However no significant difference in comparison with simulated results is expected.

Comparing the experimental and simulated residual stresses results of top and bottom sheets of each joint geometry shows little variance with similar distribution. Comparing the simulated residual stresses results for all Brezel, C-weld and Ring-weld geometries shows little variance, and from this the predictive limits of the current simulations can be seen. Whereas magnitudes within certain regions can be estimated, the simulations cannot account for the differences in heating cycle between each of the geometries. Since steel exhibits different thermal expansion rates based on its phase, some method of approximating a phase transformation could be employed to provide more detailed results.

Cooling rate values drawn from the simulated models of laser spot welds were recorded at the integration points of elements that corresponded to the potential failure locations in laser spot welds and these are listed in Table 1. Large differences can be found in the cooling rates at these locations, and this can also play an important role in the fatigue performance of the joints due to formation of brittle and metastable phases. The cooling rates found in Table 1 are generally higher at the start point of welding in the C-weld and Brezel laser welds, since the base metal acts as a large heat sink at this time while the start point of welding in the Ring-weld has a relatively low cooling rate due to the heat accumulation by the end of the weld. Similar results can be observed by comparing the cooling slopes of temperature probes 1 and 3 for corresponding weld geometries in Fig. 7. As the area around the weld is heated, a lower cooling rate is seen in the rest positions listed in Table 1. Comparing the cooling rates of positions 2 and 4, in both the Brezel and C-weld geometries, position 4, which is welded later in the cycle, has a cooling rate that is 25-65% lower than at position 2. The internal arcs that are present in the Brezel, but not in the C-weld, contribute to this effect, since they provide some pre-heating for the first exterior section, and post-heating for the last exterior section (positions 1 and 5 in Table 1, respectively) of the weld. In general, Ring-weld shows a lower cooling rate than C-weld and Brezel geometries, while Brezel type of laser spot welding can protect the start and end points of a weld against applied stress and strain, since they are within the region protected by strength overmatching (due to the shielding effect of strength overmatching on the weld region of the joint).

Understanding of the influence of heating cycle on cooling rates could be used advantageously by designing LSWs such that, where it is known that an area to one side of the weld experiences a larger fatigue loading, the weld geometry is oriented such that this section is welded later in the cycle, so that the accumulated heat results in a lower cooling rate and thus a more fatigue-resistant section of the weld. Although the different cooling rates in the sides of the weld are not a significant factor in the welding of low-carbon steels, phase transformation due to different cooling rates is important when dealing with high strength or advanced high strength steels which are seeing increasing use in the car industry.

## **5 Conclusions**

The residual stress state for 7.0 mm nugget size of resistance spot welding (RSW) was compared with that for the Ring- weld geometry of laser spot welding (LSW), using Nd:YAG laser beam welding process and 2.0 mm thick low-carbon steel sheets. Experimental and numerical residual stress and thermal analyses on three different geometries of LSW overlap joints and RSW were conducted. The following conclusions can be made:

1. In the comparison of the tangential residual stresses for RSW and LSW, LSW shows higher tensile residual stresses inside the weld ring than those found in the nugget of RSW. The weld region in LSW has been surrounded by a compressive region which is larger in magnitude than that of the RSW.
2. Good agreement can be found between experimental and simulated temperature field results, using a basic model with a volume Conical Gaussian heat source.
3. Residual stresses can be predicted qualitatively using a partially-coupled simulation which uses an isotropic hardening model and ignores the effects of phase transformations. This can be useful in determining the relative magnitudes of compressive and tensile residual stresses, but a more detailed model is required to achieve more accurate results.

4. LSW paths can be adjusted to modify the cooling rates, and thus the phase compositions, at certain points in the weld. This knowledge can be used to apply a form of local engineering to laser welded structures.
5. The Ring-weld geometry of LSW shows lower cooling rate than C-weld and Brezel geometries, while the Brezel geometry can protect start and end points of weld against applied stress and strain, keeping them in the protected region by strength overmatching

## 6 Acknowledgment

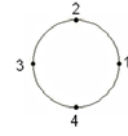
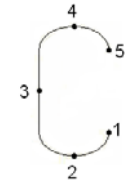
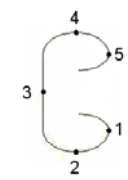
Authors wish to thank to C. H. J. Gerritsen, ArcelorMittal Research Industry Gent- Belgium for provision of the steel sheets and resistance spot welded samples.

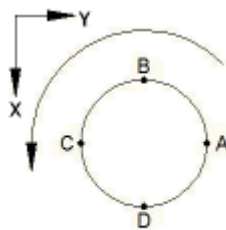
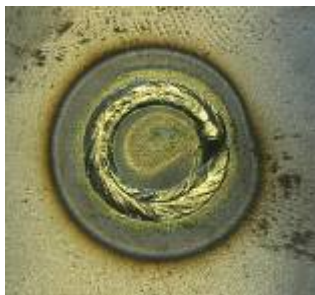
## 7 References

- [1] M. Janota, H. Neumann, *Welding in the World* 52 (2008) 12-16.
- [2] T. Schwoerer, *Joining in Automotive Enging. Conf.*, Bad Nauheim, Germany, April 2008.
- [3] D. Rosenthal, *Trans. ASME* 68 (1946) 849-866.
- [4] V. Pavelic, R. Tanbakuchi, O.A. Uyehara, Myers, *Welding J.* 48 (1969) 295-305.
- [5] J. Goldak, A. Chakravarti, Bibby: *Metallurgical Transactions B* 15b (1984) 299-305.
- [6] J. Mazumder, W.M. Steen, *Journal of Applied Physics* 51(1980) 941-947.
- [7] W. Sudnik, D. Radaj, W. Erofeew, *Journal of Applied Physics D* 29 (1996) 2811-2817.
- [8] M. Zain-ul-Abdein, D. Nelias, J.F. Jullien, D. Deloison, *J. Mater. Process. Tech.* (2008) doi:10.1016/j.jmatprotec.2008.06.051
- [9] C.L. Tsai, C.M. Tso, W. Mohr, *Geometry effect on fatigue life of fillet welds under tension-compression loading*, EWI Research Report, Report no. MR0306, 2003.

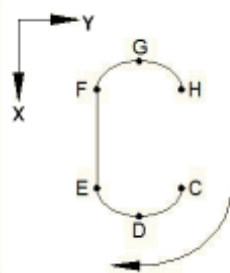
- [10] F.A. Soul, Y.H. Zhang, *Sci. Technol. Weld. Joining* 11 (2006) 688-693.
- [11] S. A. Tsirkas, P. Papanikos, Th. Kermanidis, *J. of Mater. Proc. Tech.* 134 (2003) 59-69.
- [12] K. R. Balasubramanian, N. Siva Shanmugam, G. Buvanashakaran, K. Sankaranarayanan, *Advances in Prod. Enging. and Management* 3 (2008) 93-105.
- [13] S. Daneshpour, S. Riekehr, M. Koçak, C.H.J. Gerritsen, *Sci. Technol. Weld. Joining* 14 (2009) 20-25.
- [14] D. Anand, D.L. Chen, S.D. Bhole, P. Andreychuk, G. Boudreau: *Mater. Sci. Enging. A*, 420 (2006) 199-207.
- [15] V. Hauk, *Structural and Residual Stress Analysis by Nondestructive Methods*, Elsevier, Amsterdam, 1997.
- [16] M.E. Fitzpatrick, A. Lodini, *Analysis of residual stress by diffraction using neutron and synchrotron radiation*, Taylor and Francis, London, 2003.
- [17] M.T. Hutchings, P.J. Withers, T.M. Holden, T. Lorentzen, *Characterization of residual stress by neutron diffraction*, Taylor and Francis, Boca Raton, USA, 2005.
- [18] G.A. Webster (ed.), *Polycrystalline Materials — Determination of residual stresses by neutron diffraction*, ISO/TTA3 Technology Trends Assessment, Geneva (2001).
- [19] A.J. Allen, M.T. Hutchings, C.G. Windsor, C. Andreani: *Adv. in Physics* 34 (1985) 445-473.
- [20] ABAQUS/Standard Version 6.7 User's Manual, ABAQUS Inc., Pawtucket, USA, 2007.
- [21] S. Daneshpour, S. Riekehr, M. Koçak, V. Ventske, A.I. Koruk, *Sci. Technol. Weld. Joining* 12 (2007) 508-515.

**Table 1** – FE results of cooling rates at specific positions of the laser spot welding paths

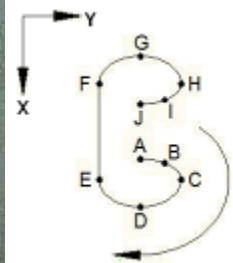
Geom.	Diagram	Position	Cooling Rate [°C s <sup>-1</sup> ]
Ring-weld		1	-272
		2	-345
		3	-257
		4	-135
C-weld		1	-1290
		2	-536
		3	-423
		4	-198
		5	-225
Brezel		1	-522
		2	-347
		3	-220
		4	-256
		5	-225



a) Ring- weld



b) C- weld



c) Brezel

**Welding  
Direction**

**Fig. 1** - Laser spot welds and schematics showing welding direction and configurations used in this study

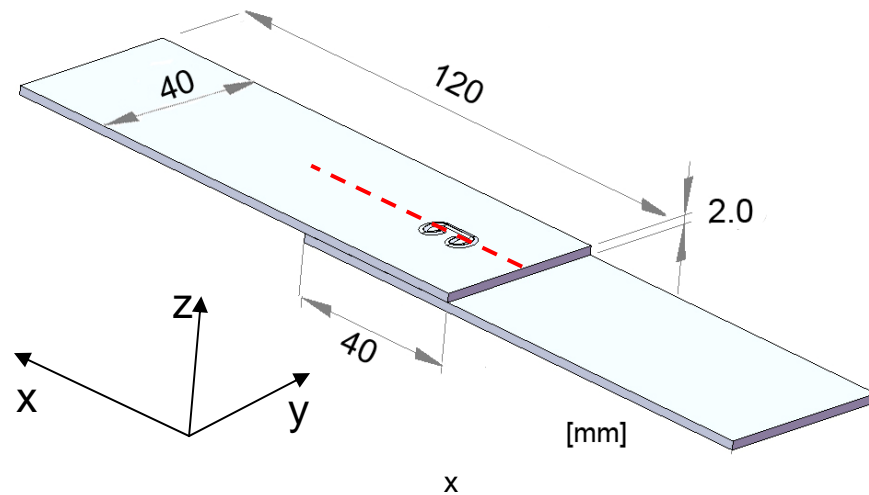


**Fig. 2** - Geometry and dimensions of laser spot welded specimens; Residual stresses were measured along the dashed line

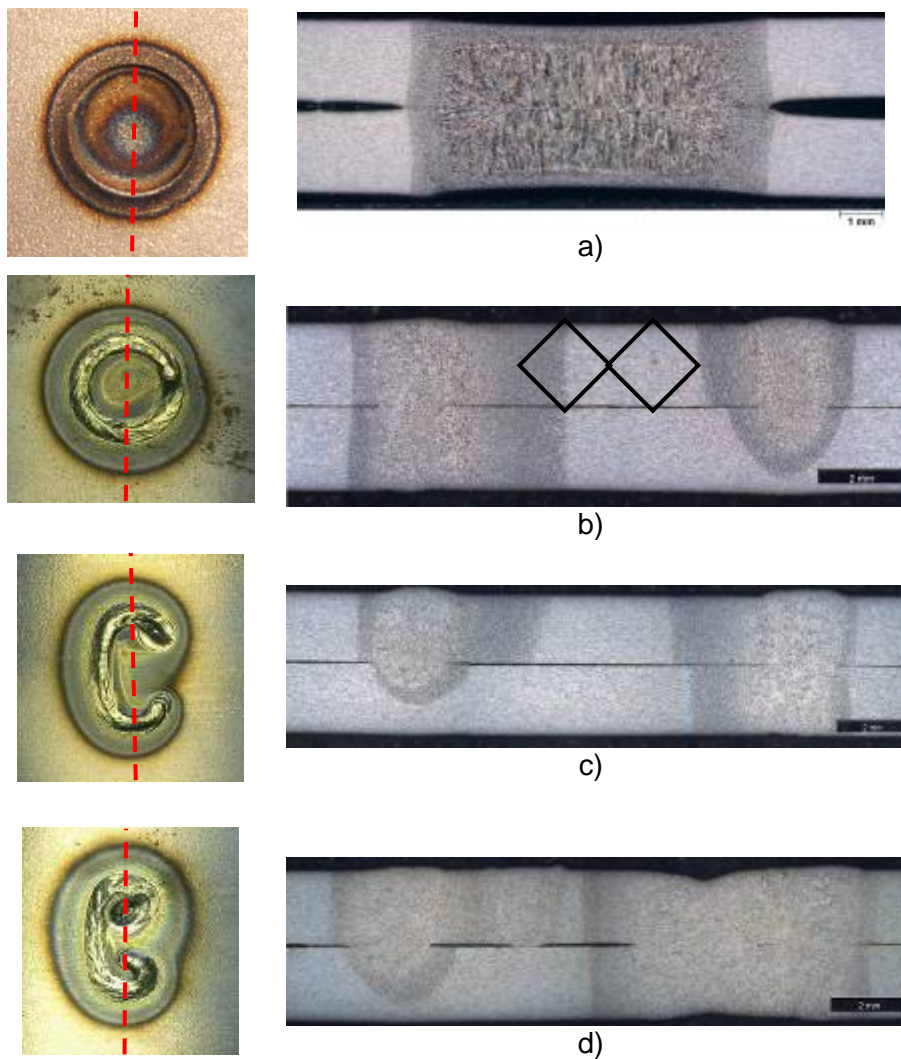
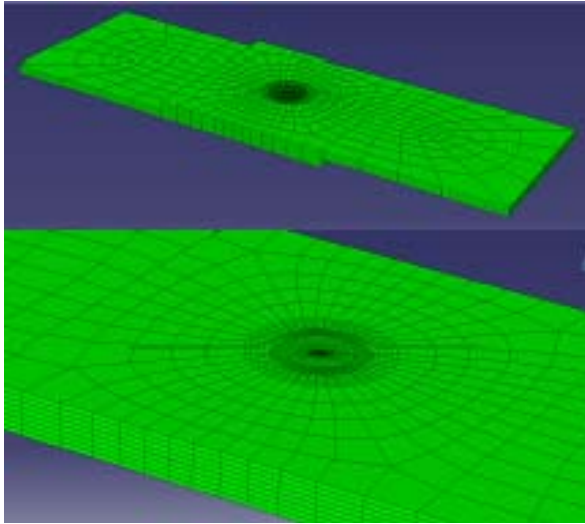
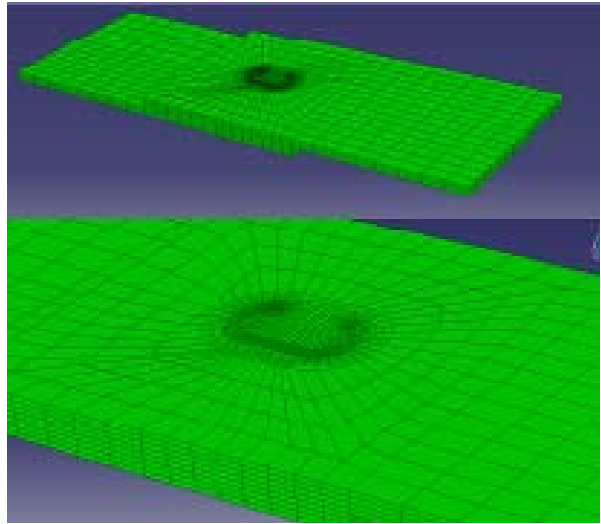


**Fig. 3** - Joint cross sections of a) Resistance spot weld, b) Ring-laser weld, c) C-laser weld and d) Brezel-laser weld specimens. Note to the full penetration of the laser welding at the end-point of the welding process. The rectangles in b) show the nominal size of the gauge volume for the experimental determination of residual stresses.

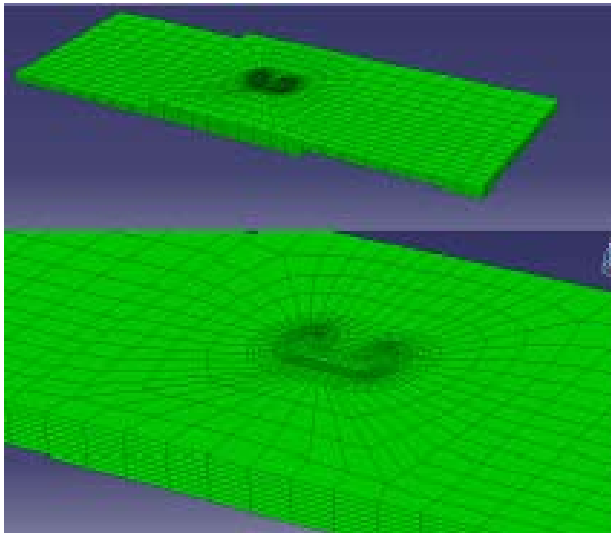




a)



b)



c)

**Fig. 4** - Meshes used for FEA of a) Ring-weld, b) C-weld and c) Brezel specimens

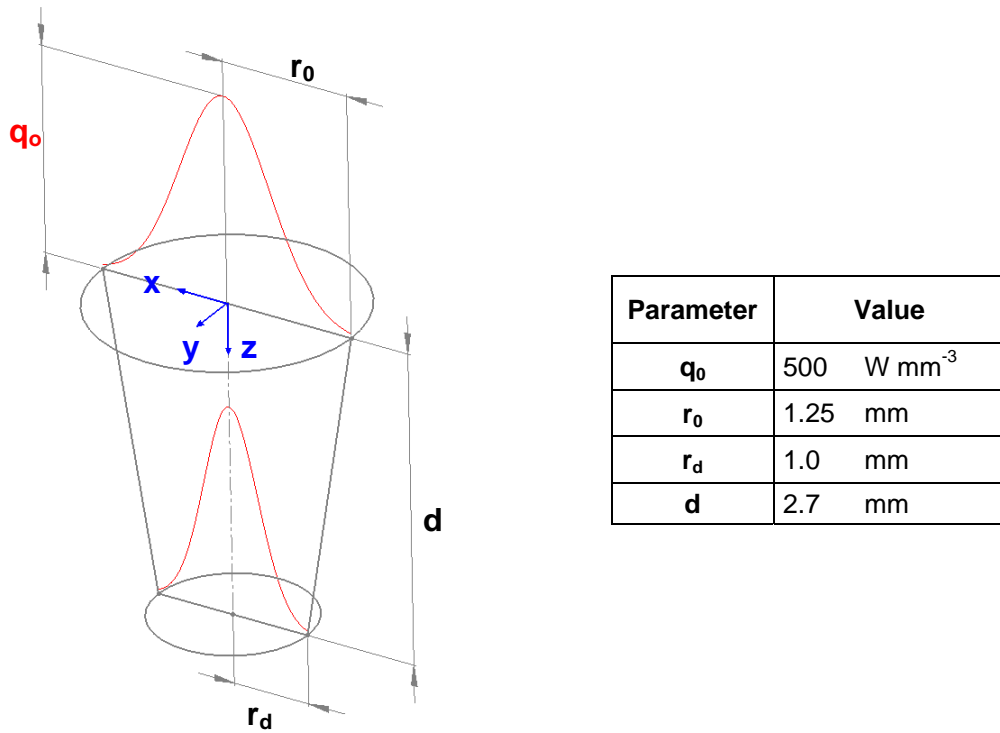


Fig. 5 - Conical Gaussian heat source diagram and heat input parameters used in this study

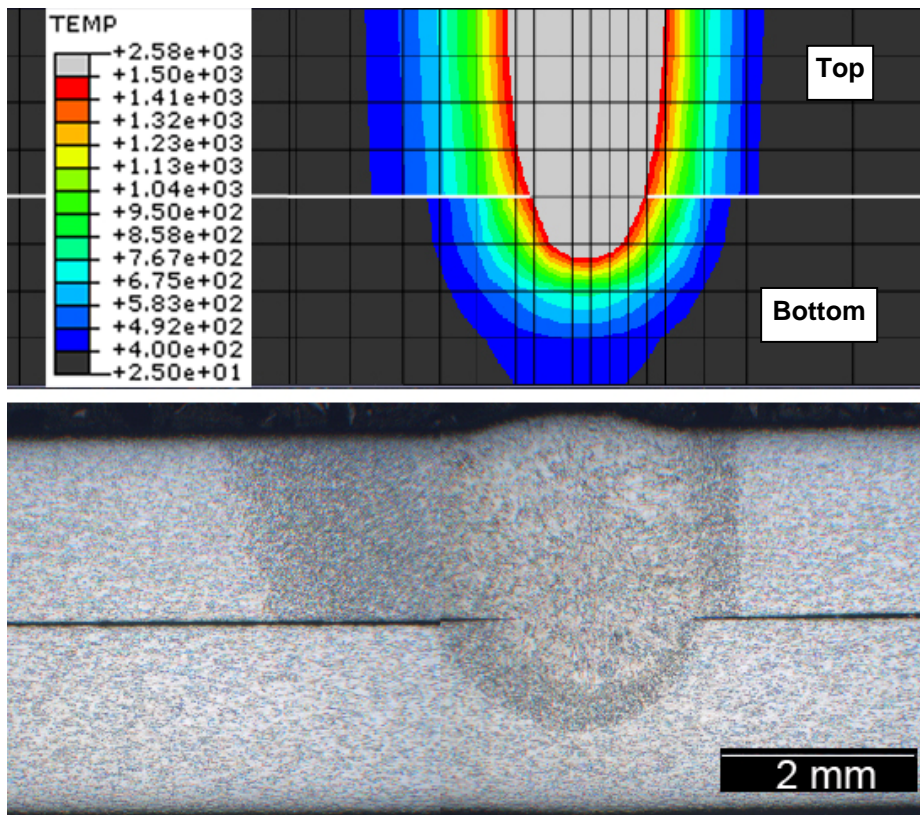
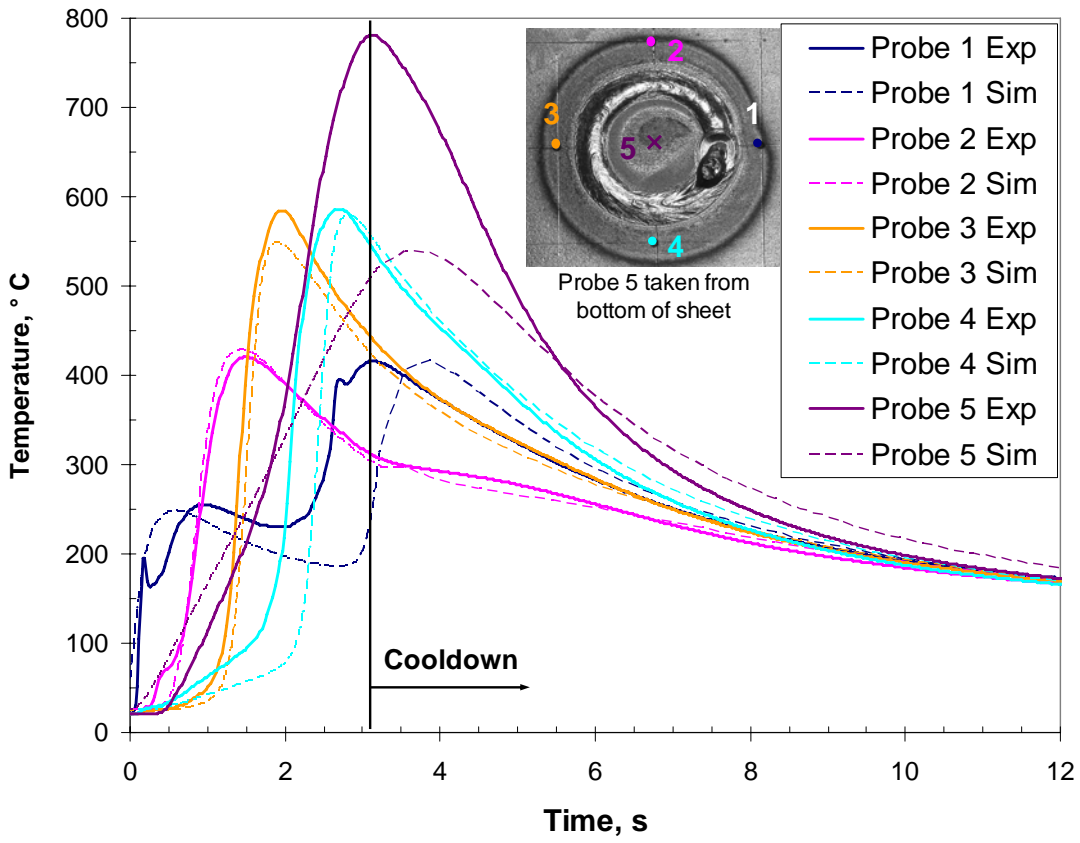
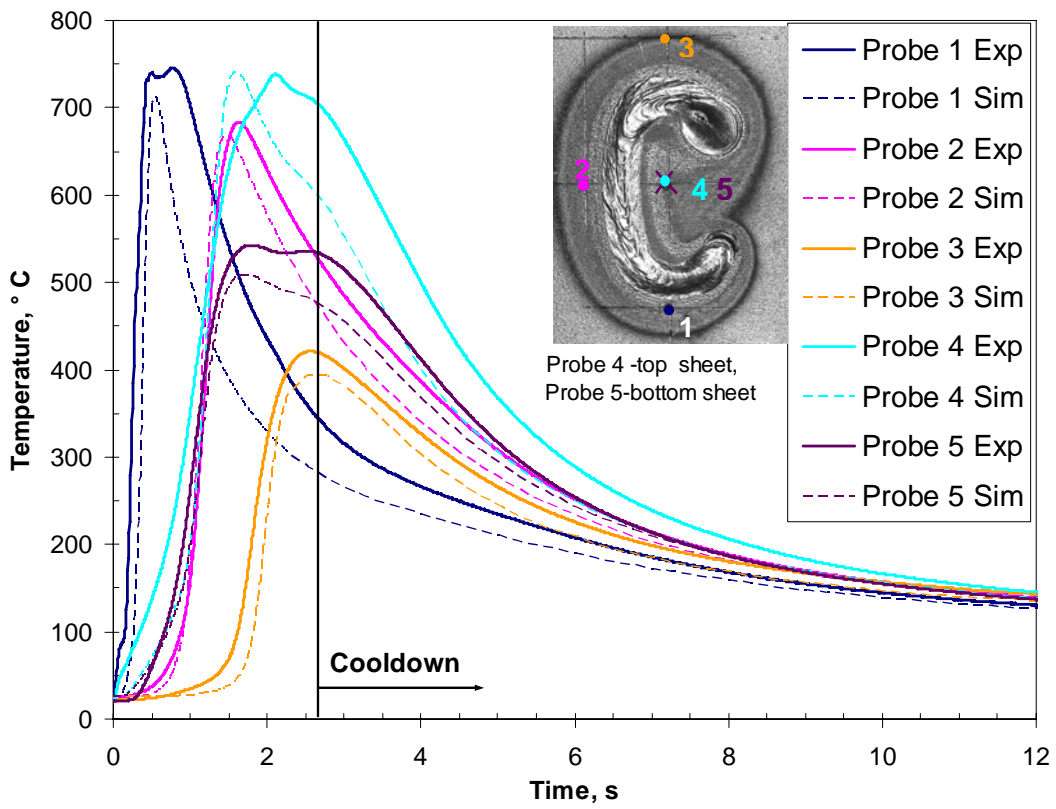


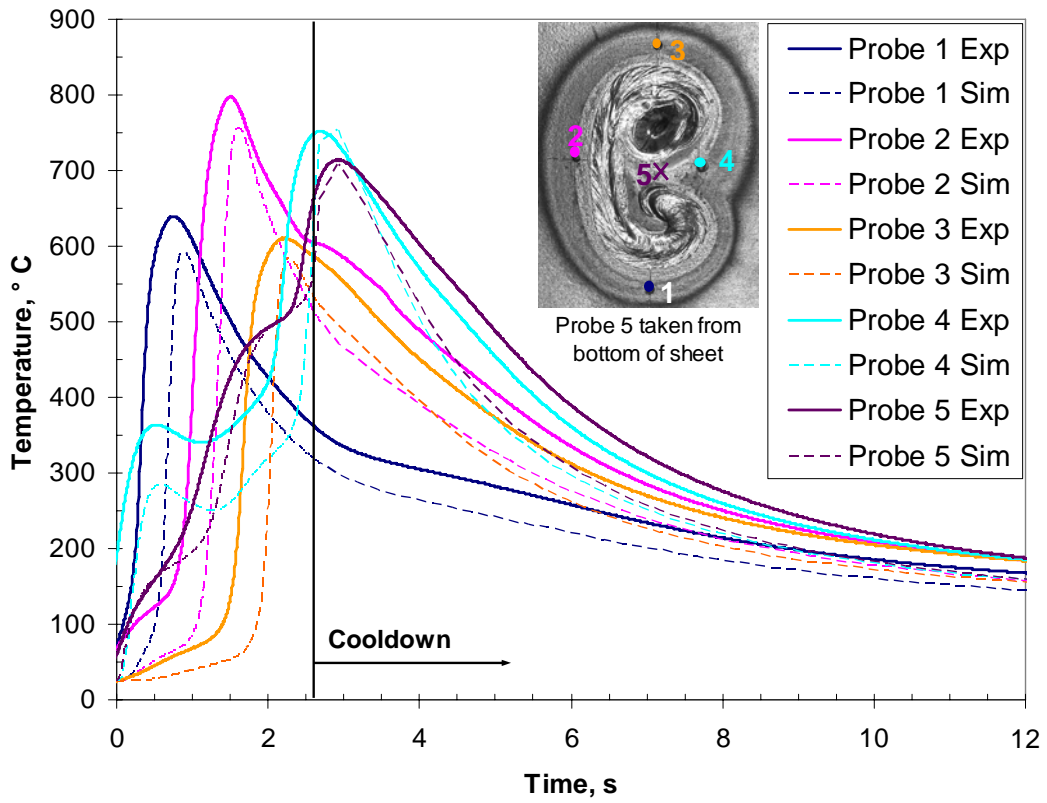
Fig. 6 - Simulated and experimental thermal cross sections



a)

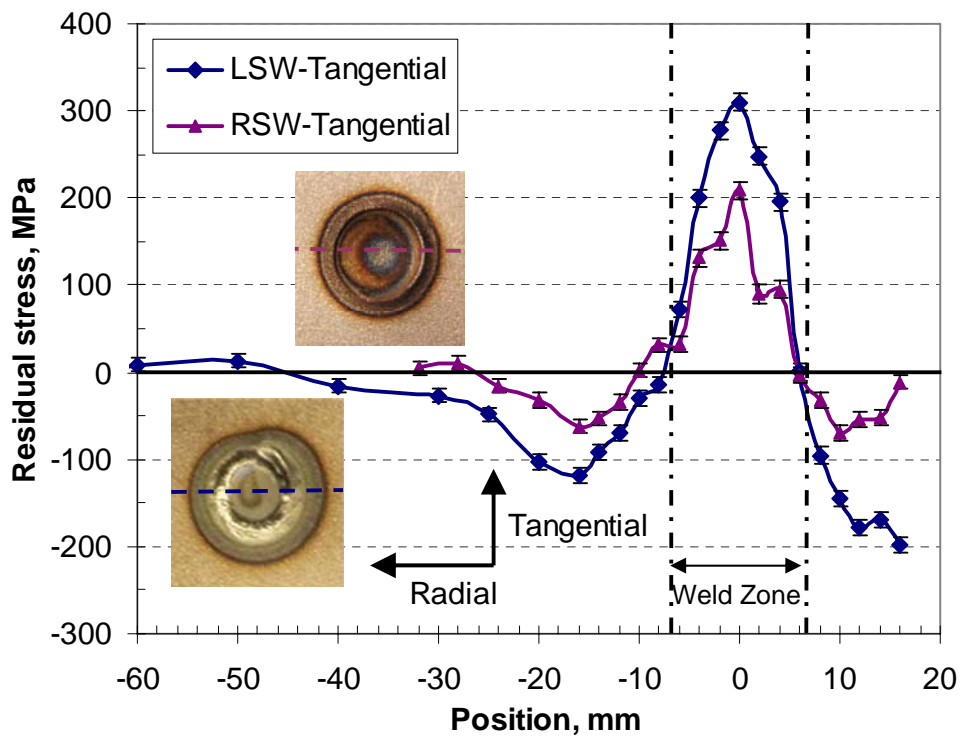


b)

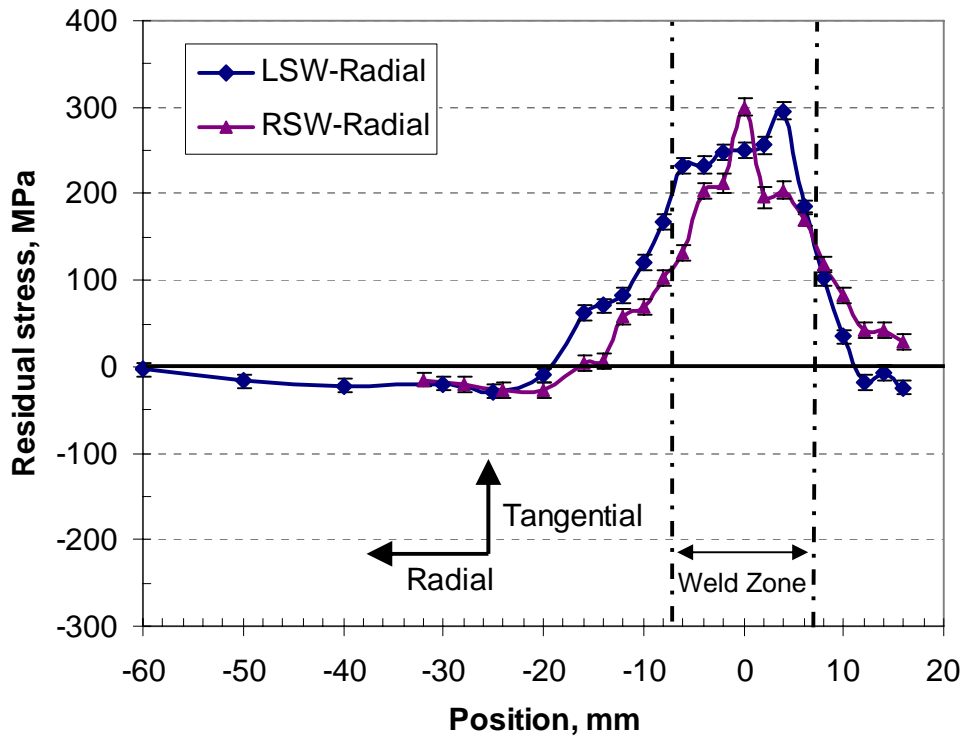


c)

**Fig. 7** - Simulated and experimental thermal histories of LSW for a) Ring-weld, b) C-weld and c) Brezel specimens

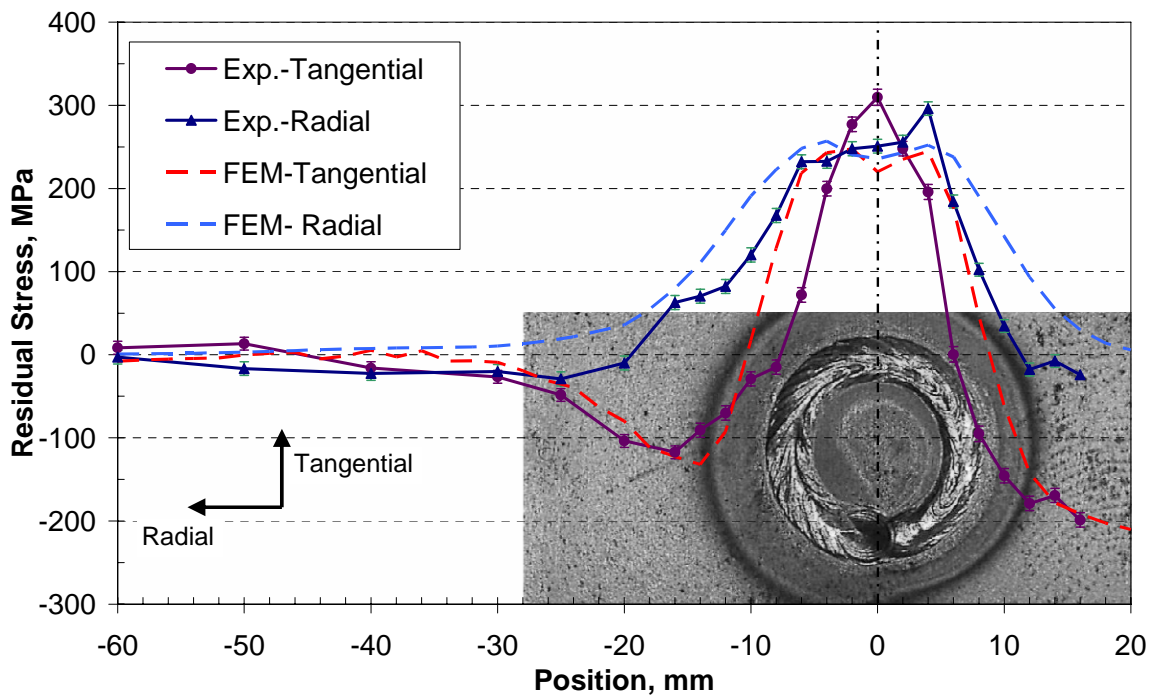


a)

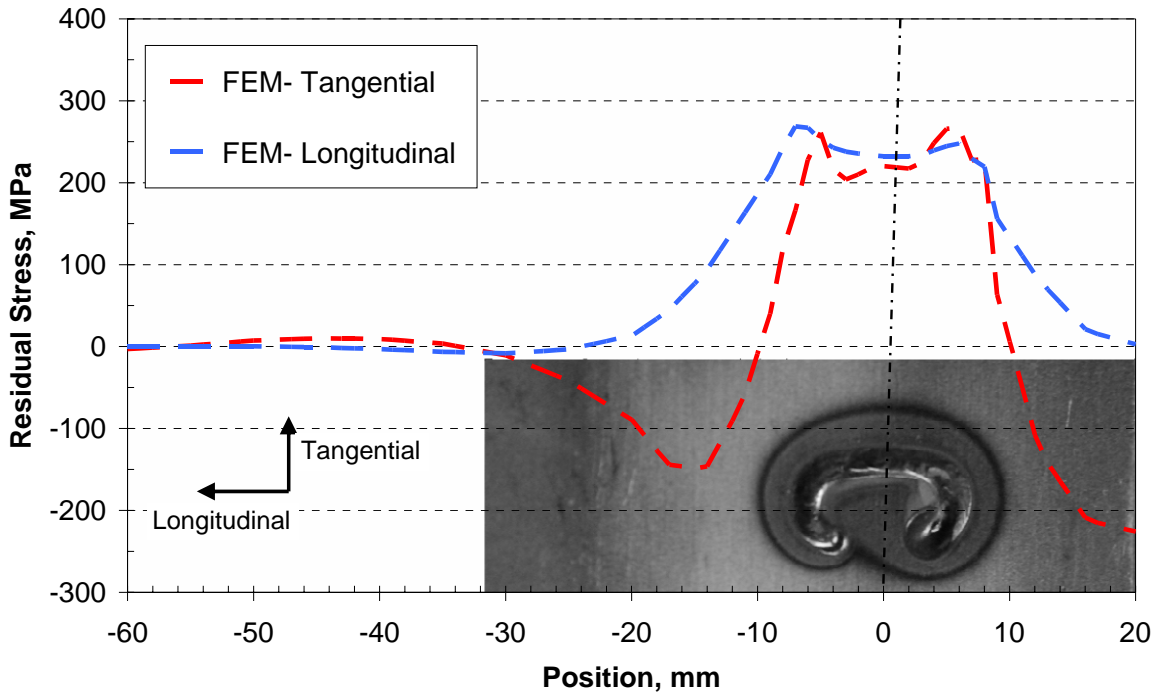


b)

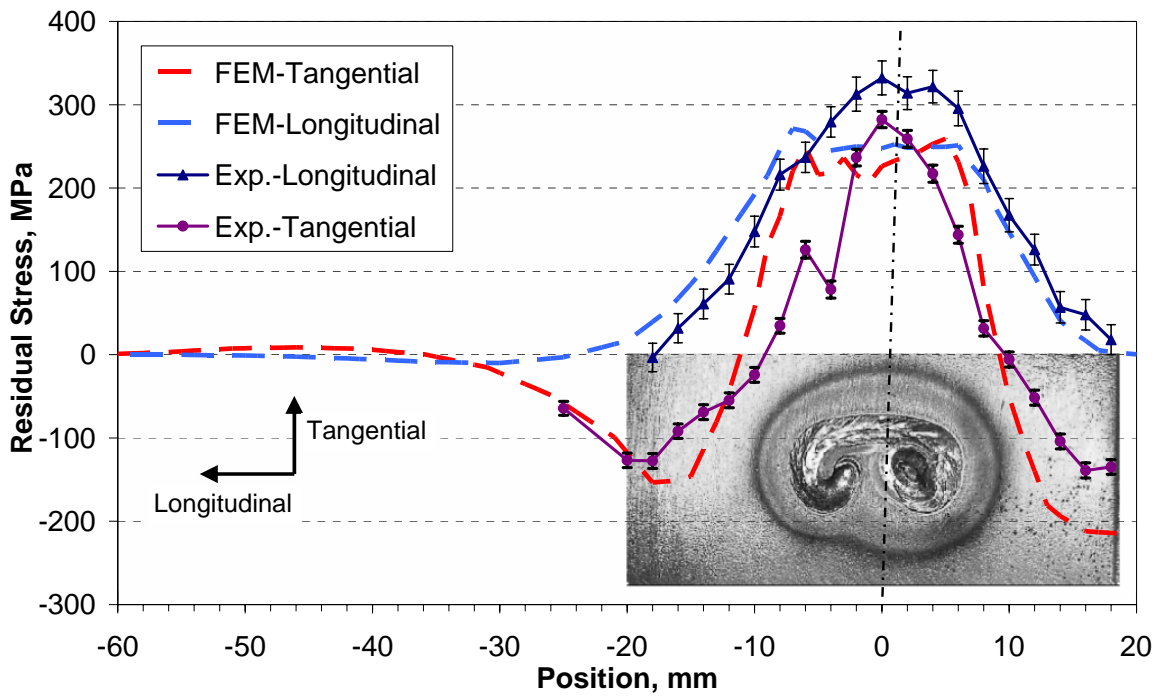
**Fig. 8** –Comparison between residual stress measurements of LSW and RSW; a) tangential residual stress and b) radial residual stress



a)



b)



c)

**Fig. 9-** Experimental and simulated residual stress distributions for a) Ring-weld, b) C-weld (FE-results only) and c) Brezel specimens